

Computational Insights into Working Mechanism of LiPF_6 Graphite Dual-Ion Battery

M.Sc. Thesis

By
SUMIT KUMAR



DISCIPLINE OF CHEMISTRY
INDIAN INSTITUTE OF TECHNOLOGY INDORE

JUNE 2019

Computational Insights into Working Mechanism of LiPF₆ Graphite Dual-Ion Battery

A THESIS

*Submitted in partial fulfillment of the
requirements for the award of the degree
of*
Master of Science

by
SUMIT KUMAR



DISCIPLINE OF CHEMISTRY
INDIAN INSTITUTE OF TECHNOLOGY INDORE
JUNE 2019



INDIAN INSTITUTE OF TECHNOLOGY INDORE

CANDIDATE'S DECLARATION

I hereby certify that the work which is being presented in the thesis entitled **Computational Insights into Working Mechanism of LiPF₆ Graphite Dual-Ion Battery** in the partial fulfillment of the requirements for the award of the degree of **MASTER OF SCIENCE** and submitted in the **DISCIPLINE OF CHEMISTRY, Indian Institute of Technology Indore**, is an authentic record of my own work carried out during the time period from July 2018 to June 2019 under the supervision of **Dr. Biswarup Pathak**, Associate Professor, Discipline of Chemistry, IIT Indore.

The matter presented in this thesis has not been submitted by me for the award of any other degree of this or any other institute.

**Signature of the student with date
(Sumit Kumar)**

This is to certify that the above statement made by the candidate is correct to the best of my/our knowledge.

**Signature of the Supervisor of M.Sc. thesis (with date)
(Dr. Biswarup Pathak)**

Sumit Kumar has successfully given his M.Sc. Oral Examination held on

Signature of Supervisor of MSc thesis
Date:

Convener, DPGC
Date:

Signature of PSPC Member 1
Date:

Signature of PSPC Member 2
Date:

Acknowledgements

With great pleasure, I want to express my deep sense of gratitude to my supervisor Dr. Biswarup Pathak, for the wonderful opportunity to pursue research and believing my research abilities. His constant guidance, support, and motivation have been immensely helpful to complete this M.Sc. project. His enthusiasm and dedication have always inspired me. Further, I would like to thank my PSPC members Dr. Sanjay Kumar Singh and Dr. Shaikh M. Mobin for their valuable suggestions and support.

I wish to express my gratitude to Prof. Pradeep Mathur, Director, IIT Indore for his continuous encouragement, help, and support in every aspect.

I am grateful to Dr. Amrendra Kumar Singh (Head, Discipline of Chemistry, Indian Institute of Technology Indore) for his suggestions and guidance in various aspects. I am also grateful to Dr. Sampak Samanta, Dr. Chelvam Venkatesh, Dr. Anjan Chakraborty, Dr. Tridib Kumar Sarma, Dr. Suman Mukhopadhyay, Dr. Apurba Kumar Das, Dr. Rajneesh Misra, Dr. Sanjay Kumar Singh, Dr. Tushar Kanti Mukherjee, Dr. Satya S. Bulusu, Dr. Abhinav Raghuvanshi and Dr. Dipak Kumar Roy for their guidance and help during various activities.

I would like to extend my sincere thanks to my great mentor Preeti Bhauriyal for her kind and friendly nature and help in dealing with difficulties.

I extend my deep thanks to my group members Dr. Kuber Singh Rawat, Dr. Surajit Nandi, Priyanka Garg, Sourabh Kumar, Preeti Bhauriyal, Gargee Bhattacharyya, Chiranjit Mondal, Akhil S Nair, Shyama Charan

Mandal, Rameshwar Lal Kumawat, Sandeep Das, Arunendu Das and Surya Sekhar Manna for their selfless co-operation and help to make my work successful.

I personally want to extend my thanks to my batch mates who were always there and never let me down during these M.Sc. days. Here, it is to be specially mentioned that, it has been wonderful to work with many Ph.D. seniors during my M.Sc.

Most importantly none of this would have been possible without the support of my family and I deeply express my love and gratitude to my Parents.

Finally, I would like to express my thanks to IIT Indore for infrastructure and all others who helped and supported me directly or indirectly.

**DEDICATED TO
MY FAMILY
AND
ALL WELL- WISHERS**

Abstract

The emerging field of dual-ion batteries (DIBs) show quite better advantages compared to the commercial Li-ion batteries in terms of high working voltage, high energy density and low cost. To improve performance, the on-going experimental studies of DIBs require a clear understanding of the reaction mechanism occurring during both charging and discharging processes as well as the resulting structural variation in the involved anions and cathode system. Therefore, in this work using the first principle calculations, we have studied the staging mechanism of PF_6^- intercalation from organic electrolyte into graphite. We have modelled four different stages stage-1, stage-2, stage-3 and stage-4 of PF_6^- intercalated graphite with four varying concentrations. The binding energy characteristics of all stages indicates the favorable intercalation of PF_6^- into graphite. The cell voltage is determined in range 5.28 to 5.49 V at specific capacity 124 mAhg^{-1} , in good agreement with experimental values. Through charge transfer analysis, we found that there is significant amount of charge transfer from graphite to PF_6^- , which clarify the PF_6^- intercalation into graphite is charging process. For high charging/discharging rates battery electrodes ought to have metallic character (for fast electron transfer) and low diffusion barrier (for fast ion transfer). Our density of states calculations confirms the metallic character of PF_6^- intercalated graphite system and from the diffusion barrier calculations, we observe that PF_6^- diffuse with an energy barrier of 0.14 eV, low enough to provide trouble free diffusion. These all results provide the clear understanding of PF_6^- intercalation into graphite and also describe the role of staging behavior to obtain the precise values of electrochemical properties.

Table of contents

	Page no.
List of figures	xi
List of tables	xiii
Chapter-1: 1. Introduction	1-3
Chapter-2:2.1. Computational methods and approximations	
➤ 2.1.1. The Schrödinger equation	4-5
➤ 2.1.2. Density functional theory	5
➤ 2.1.3. Exchange-correlation functional	5-6
▪ 2.1.3.1. The local density approximation (LDA)	6
▪ 2.1.3.2. The generalized gradient approximation (GGA)	6-7
➤ 2.1.4. The projector augmented wave method (PAW)	7
2.2. Computational details	7-8
Chapter-3: 3. Results and discussion	
➤ 3.1. Geometric structure and stable binding sites	9-10
➤ 3.2. System Setup	10-13
➤ 3.3. Binding energy of PF ₆ ⁻ intercalated graphite stages	13-15
➤ 3.4. X-ray diffraction study of PF ₆ ⁻ intercalation into graphite	16-17
➤ 3.5. Electrochemical characteristics	17-20
➤ 3.6. Electronic properties	20-22
➤ 3.7. PF ₆ ⁻ diffusion and energy profile along minimum energy paths	22-23
Chapter-4: 4. Conclusion	24-25
References	26-30

List of figures

	Page No.
Figure 1. Different orientation on PF_6^- intercalation: (a) three fluorine atoms facing graphene and (b) two fluorine atoms facing graphene. Optimized structures of PF_6^- intercalation at three different sites with three fluorine atoms facing graphene: (c) S1, (d) S2, (e) S3.	10
Figure 2. Systematic representation of staging mechanism of PF_6^- intercalation into graphite (a) stage-4, (b) stage-2, (c) stage-1. Relative energy (RE) is in eV units for systems containing same PF_6^- concentration.	12
Figure 3. Schematic representation of the optimized structures of four different PF_6^- intercalated graphite stages: (a) stage-1, (b) stage-2, (c) stage-3, (d) stage-4.	13
Figure 4. Simulated XRD pattern of pristine graphite and different stages of PF_6^- intercalated graphite supercells.	17
Figure 5. Staging voltage profile diagram for PF_6^- intercalated graphite system.	19
Figure 6. (a) Total DOS and projected DOS of PF_6^- intercalated graphite. The Fermi level is set at zero. (b) Isosurface ($0.002 e \text{ \AA}^{-3}$) for the charge density difference for PF_6^- intercalated graphite system.	22
Figure 7. (a) Systematic representation of optimized diffusion pathways of PF_6^- in graphite and (b) involved energy barriers corresponding to the diffusion pathways.	23

List of tables

	Page No.
Table 1. Binding energy (eV) per PF_6^- and average interlayer distance (\AA) for all stages with different PF_6^- concentration.	15

Chapter 1

Introduction

To fulfil future energy demands, it is very essential to search for cost-effective and durable energy sources which can also provide high energy outputs. In this regard, rechargeable metal-ion batteries have emerged as one of the important energy sources that have attracted quite a great attention of the scientific community thanks to their high energy density, suitable discharge voltage and high capacity. Also, with the on-going developments, the rechargeable Li-ion batteries (LIBs) currently cover the battery market for mobile phones, laptops, e-readers and many other electronic gadgets. However, the cost and safety issues associated with LIBs limit their suitability for grid-scale applications. Therefore, there is a constant urge for other energy storage options, and in this consideration, the dual ion batteries (DIBs) can be the ideal choice. The DIBs offer high working voltage, high energy density, and low cost because of which they can meet the requirements of electric vehicles and grid scale applications [1]. The working mechanism of DIBs involves the intercalation of anions into cathode, whereas the intercalation or electroplating of cations into anodes during charging process, and the reverse processes occur during discharge. The very first anion intercalation into graphite was reported by Rudorff and Hofmann in 1938, where the intercalation of HSO_4^- and ClO_4^- anions was observed from acid electrolytes [2]. After that, in 1989, for the first time McCullough et al. reported a DIB, also termed as dual-graphite battery as graphite was used as both anode and cathode in the non-aqueous electrolyte involving the intercalation/deintercalation of ClO_4^- . Because of the promising properties, the DIBs are being constantly explored and researchers are continuously trying to increase the battery performance by varying the electrodes [3–5], electrolytes [6–9] and other important components like current collectors and separators. With the progressive research inputs, several forms of carbon have been explored towards their

cathode applicability such as soft carbon, foam graphite, mesocarbon microbead and natural graphite [10–13]. Whereas, for dual-ion battery anodes, both graphite and metal anodes have been studied extensively [10,14]. The dual ion batteries with metal anodes are one of the current interests as they are the promising alternatives of graphite offering high voltage, cycle life, suitable storage capacity due to their new redox chemistry. The metal anode gets alloyed/de-alloyed with cation present in the electrolyte and this alloy/de-alloy process store higher amount of energy as compared to intercalation/deintercalation mechanism in graphite [15]. In 2011, Zhang compared the electrochemical properties of different metals as anode material (Al, Mg, Zn, Sb, Bi and Sn) for LIBs where Li metal showed the highest theoretical specific capacity. Till present, various metal anodes have been proposed for dual-ion batteries such as Li, Na, K, Ca, and Al, but focus has still been on Li metal anode, as the Li-dual-ion batteries can supply highest working voltage due to lowest redox potential of Li-plating/dissolution reactions [16]. Other than the exploration of anodes and cathodes, the researchers have also studied a series of anions such as BF_4^- , AlCl_4^- , PF_6^- , bis(fluorosulfonyl)imide (FSI), bis(trifluoromethanesulfonyl) imide (TFSI) towards their intercalation behaviour into cathodes in DIB applications. Among these anions, the PF_6^- secures an important place as this is one of the most explored anion in DIBs due to its chemical and electrochemical inertness against cell components, high anti-oxidation ability, suitable size for insertion into graphite and high diffusivity of PF_6^- in graphite [17–19]. One of the very recent study is reported by Wang et al. proposing a Li-ion DIB which offers a very high average voltage of 4.6 V and specific capacity of 99.4 mAhg^{-1} with superior cycling stability and very high coulombic efficiency. This dual-ion battery consists of graphite cathode, Li anode and an organic liquid electrolyte (lithium hexafluorophosphate (LiPF_6) in ethyl methyl carbonate (EMC)), where, PF_6^- reversibly intercalates and de-intercalates between the graphite layers. However, till present, most of the studies

carried out in the field of PF₆-DIB are experimental, which do provide promising results but could not give much information about the involved reaction mechanisms, the qualitative and quantitative interaction approach of PF₆⁻ with graphite cathode and the structural changes that occur after intercalation in both PF₆⁻ and graphite. Therefore, at this developing stage of PF₆-DIBs, the theoretical prospective are highly sought that can be helpful to researchers to perfectly understand the undergoing reaction mechanism, the role of electrodes and electrolytes in battery performance, charge transfer mechanism and theoretical voltage profile and specific capacity. So, in this work, we have used the first-principles methods within the density functional theory to investigate the PF₆⁻ intercalation into graphite. Utilizing the staging phenomenon of anion intercalation into graphite, we have explored the properties of PF₆⁻ intercalated graphite including the geometric structure, stability, and also calculated the crucial electrochemical properties such as the theoretical storage capacity and average voltage. The electronic properties, density of state, charge density difference and Bader charge analysis processes are used to study the charge transfer mechanism between graphite and PF₆⁻. Further, the diffusion pathways of PF₆⁻ inside the graphite has been investigated to check the rate performance of the battery. Moreover, for the better understanding of the DIB working mechanism, the necessary comparisons of the theoretical analysis have been made with the experimental results.

Chapter 2

Computational methods

2.1. Computational methods and approximations

2.1.1. The Schrödinger equation

The Schrödinger equation of multi-electron systems is the foundation of theoretical chemistry. It is a mathematical equation, which is used for calculating the properties of solids, atoms and molecules. Two forms of Schrödinger equation exist, which are time-independent and time-dependent Schrödinger equation. Commonly, time-independent Schrödinger equation is used for calculating the properties of a matter.

Let's consider a multi-electron system. The time independent Schrödinger equation is given as,

$$H\Psi(x_1, x_2, x_3, \dots, x_n, r_1, r_2, r_3, \dots, r_n) = E\Psi(x_1, x_2, x_3, \dots, x_n, r_1, r_2, r_3, \dots, r_n) \quad (2.1)$$

Here, $x_1, x_2, x_3, \dots, x_n$ are the position coordinates of multi electrons and $r_1, r_2, r_3, \dots, r_n$ are the position coordinates of nuclei.

For multi-electron system, Hamiltonian operator will be written as

$$H = T_e + T_n + V_{ee} + V_{nn} + V_{ne} \quad (2.2)$$

Here, T_e and T_n are the kinetic energy of electrons and nuclei, respectively. V_{ee} is the inter-electronic repulsion potential, V_{nn} is the inter-nuclei repulsion potential, and V_{ne} is the attractive potential between electrons and nuclei.

So, the Hamiltonian operator can be written in the extended form as,

$$H = -\frac{\hbar^2}{2m_e} \sum_{i=1}^n \nabla_i^2 - \frac{\hbar^2}{2} \sum_{l=1}^m \frac{\nabla_l^2}{m_l} + \sum_{i=1}^n \sum_{j>i}^m \frac{e^2}{r_{ij}} + \sum_{l=1}^m \sum_{j>l}^m \frac{z_l z_j e^2}{r_{lj}} - \sum_{i=1}^n \sum_{l=1}^m \frac{z_l e^2}{r_{il}} \quad (2.3)$$

For multi-electron systems, Schrödinger equation becomes very complicated and cannot be solved practically. So, some approximations are required, and Born-Oppenheimer is the first, and one of the most important approximation studied to decrease the Schrödinger equation's complication. According to Born-Oppenheimer approximation, the dynamics of electrons and nuclei can be separated as during the motion of electrons, the position of nucleus seems constant due to the very large gap between their atomic masses ($m_{\text{nuclei}} \gg m_e$). so, the wavefunction can be decoupled into electronic and nuclear parts as follows,

$$\Psi(x_1, x_2, x_3, \dots, x_n, r_1, r_2, r_3, \dots, r_n) = \Psi(x_1, x_2, x_3, \dots, x_n) \Psi(r_1, r_2, r_3, \dots, r_n) \quad (2.4)$$

And the kinetic energy terms for nuclei in the Hamiltonian operator can be neglected. So, the equation becomes

$$H = -\frac{\hbar^2}{2m_e} \sum_{i=1}^n \nabla_i^2 + \sum_{i=1}^n \sum_{j>i}^m \frac{e^2}{r_{ij}} - \sum_{i=1}^n \sum_{l=1}^m \frac{z_l e^2}{r_{il}} \quad (2.5)$$

2.1.2. Density functional theory:

Schrödinger equation cannot be solved easily for multi electron system due to its dependence on $3n$ (n is the no. of electrons) positional coordinates. So, many quantum-mechanical modelling theories were developed among them DFT is the most widely used modelling method in computational chemistry and material science. DFT uses electron density for its calculations, which only depends upon three positional coordinates. Thomas and Fermi proposed this innovative idea for non-interacting system of free electron gaseous molecules. Then, the two theorems proposed by Hohenberg and Kohn employing the electron density, are highly useful in DFT calculations. DFT is used to investigate the electronic structure of a matter using the quantum-mechanical methods. It predicts a variety of molecular properties like molecular structure, magnetic and electronic behaviour, vibrational frequencies, and many more.

2.1.3. Exchange-correlation functional

Kohn and Sham proposed an energy equation for many body problems by replacing the many body system with non-interacting system. Kohn-Sham energy equation is as follows,

$$E[\{\Psi\}] = E_{known}[\{\Psi\}] + E_{xc}[\{\Psi\}] \quad (2.6)$$

Here, the equation (2.6) consists of two parts, one is known part and the other one is unknown part. This unknown parameter is known as exchange correlation functional. This E_{xc} unknown term can further be divided into

two parts one is correlation and another one is exchange part. Therefore, E_{xc} can be written as,

$$E_{xc}(n(\mathbf{r})) = E_x(n(\mathbf{r})) + E_c(n(\mathbf{r})) \quad (2.7)$$

Based on the above equation (2.7), different approximations are used for solving the exchange correlation term. Two main approximations for exchange correlation functional are discussed below.

2.1.3.1. The local density approximation (LDA)

Homogeneous gas of the electron has been considered for this exchange correlation functional. However, this is represented as follow,

$$E_{xc}^{LDA} = \int d^3r n(\mathbf{r}) \mathcal{E}_{xc}^{hom}(n(\mathbf{r})) \quad (2.8)$$

In the above equation (2.8) $\mathcal{E}_{xc}^{hom}(n(\mathbf{r}))$ and $n(\mathbf{r})$ are the average exchange correlation energy and homogeneous electron density, respectively.

Here, homogeneous electron density is the addition of the ρ_α and ρ_β (spin densities of the electron) which is local spin-density approximation (LSDA).

$$\rho = \rho_\alpha + \rho_\beta \quad (2.9)$$

This gives better results than HF and generally used for solid materials. However, it is not good enough for the calculation of band gap, bond dissociation energy, and so on.

2.1.3.2. The generalized gradient approximation (GGA)

Due to the limited applicability of LDA, researchers have come across Generalized gradient approximation (GGA). In this case, the electron density gradient is used, and the equation (2.8) is rewritten as follows,

$$E_{xc}^{GGA} = \int d^3r n(\mathbf{r}) \mathcal{E}_{xc}^{GGA}(n(\mathbf{r}), \nabla n(\mathbf{r})) \quad (2.10)$$

This GGA gives very accurate results compared with the LDA. Moreover, GGA developed Perdew, Burke and Ernzerhof (PBE) functional is used which is as follow,

$$E_x^{PBE} = \int d^3r n(\mathbf{r}) \varepsilon_x^{PBE}(n(\mathbf{r}), s(\mathbf{r})) \quad (2.11)$$

In this context, multiplying by a factor F_x^{PBE} with LDA gives PBE. Moreover, the factor F_x^{PBE} is dependent on $s(\mathbf{r})$. Hence, it will look like as,

$$\varepsilon_x^{PBE}(n(\mathbf{r}), s(\mathbf{r})) = \varepsilon_x^{LDA}(n(\mathbf{r})) * F_x^{PBE}(s(\mathbf{r})) \quad (2.12)$$

However, some other GGA approximations also give accurate results like Perdew and Wang (PW91), PBEsol, revised PBE, and so on.

2.1.4. The projector augmented wave method (PAW)

Due to the presence of two different kinds of electrons (core and valence electrons) in an atom two different wavefunctions are present. These two different wavefunctions are represented by two different basis sets. Valence electrons are represented by plane wave basis sets whereas core electrons cannot be represented by plane wave basis sets due to high computational cost. Therefore, the PAW method is used to describe the core electrons. It uses a linear transformation operator, T which transform electronic wave function to pseudo electronic wave function. We have used the PAW method as implemented in Vienna ab-initio simulation (VASP) package.

2.2. Computational details

We have used the first-principles calculations as implemented in the Vienna Ab initio simulation package (VASP) for all the structures [20,21]. The generalized gradient approximation of Perdew-Burke-Ernzerhoff (GGA-PBE) is used to describe the exchange-correlation potential [22] and to treat the interaction between core and valence electrons, projector augmented-wave (PAW) [23] method is used. A cut-off energy of 470 eV is used for plane-wave basis set for all the calculations. During structural optimization, the Brillouin zone was sampled with a gamma centred k-point grid of $7 \times 7 \times 7$ for unit cell and $3 \times 3 \times 1$ for supercell calculations. All the structures are optimized with total energy convergence criteria of 10^{-5} eV/Å and fully relaxing the atomic and lattice positions until the

Hellmann-Feynman forces on all the atoms were less than 0.01 eV/Å. DFT-D3 approach has been used for van der Waals corrections [24]. For density of state (DOS) calculations, a 3×3×1 supercell is used with a k-point grid of 15×15×15. The Bader charge analysis [25–27] was performed for quantitative determination of charge transfer from graphite to PF₆⁻ molecule. We have calculated the diffusion barriers using the climbing image nudge elastic band method (CI-NEB) [28]. The minimum energy paths (MEP) are designed by introducing seven structural images between initial and final structures. The energy convergence criteria are set at 10⁻³ eV. Zero-point energy (ZPE) correction is also included in the diffusion barrier calculations which is calculated as, $ZPE = \sum \frac{h\nu_i}{2}$, where, h is Planck's constant and ν is the vibrational frequency. ZPE is calculated by considering the degree of freedom of intercalated PF₆⁻.

Chapter 3

Results and discussion:

3.1. Geometric structure and stable binding sites

In DIBs, it has been reported that anions get intercalated and deintercalated into the cathode electrode. This intercalation and deintercalation can lead to structural changes. So, it is quite necessary to determine the changes occurring in the geometry structure of PF_6^- on intercalation into graphite. We observe that after intercalation, the perfect octahedral geometry of PF_6^- (90° $\angle\text{F-P-F}$ bond angle and 1.64 \AA P-F bond length) gets slightly distorted with $\angle\text{F-P-F}$ bond angle in the range of $89.63^\circ - 90.37^\circ$ and P-F bond length of 1.63 \AA . This distortion could be the result of the acting van der Waals forces between layers of graphite as well as the interactions between the host graphite layers and PF_6^- .

Further, to investigate the PF_6^- intercalation into graphite, it is crucial to examine the possible orientation and intercalation sites. PF_6^- can opt three different orientations on intercalation, (a) one fluorine atom facing host graphite layer, (b) two fluorine atoms facing host graphite layer, (c) three fluorine atoms facing host graphite layer. Out of these, the three fluorine atoms facing orientation is the most stable. Next, we examine the stable intercalation sites of PF_6^- into graphite. We find that three intercalation sites, (a) S1, (b) S2, and (c) S3 are stable. In the S1 site, the phosphorus atom occupies the top of C atoms. Whereas in the S2 site, phosphorus atom occupies the C-C bond bridge position and in S3 site, phosphorus atom is present in the hollow region. The optimized geometries and relative energies of all three sites are shown in Figure 1. These sites are very close in energy with S1 site being the most stable site for PF_6^- intercalation.

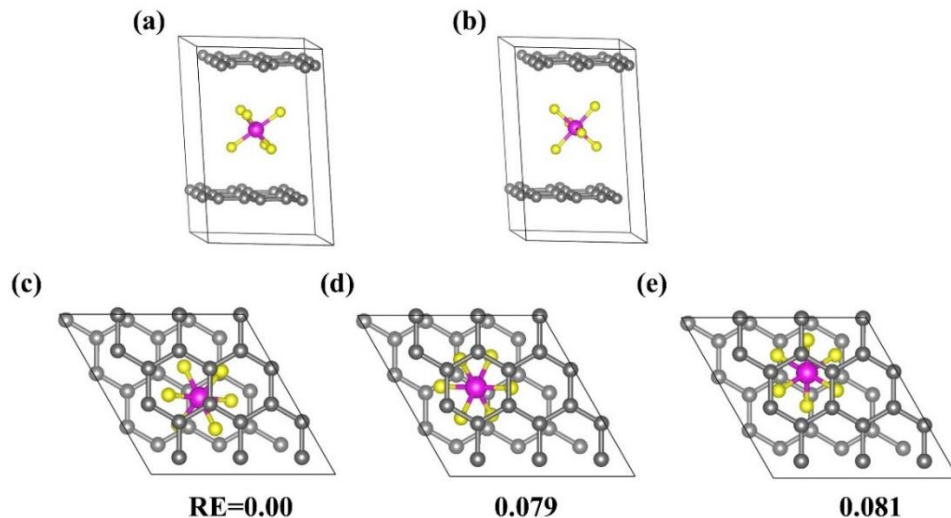


Figure 1. Different orientation on PF_6^- intercalation: (a) three fluorine atoms facing graphene and (b) two fluorine atoms facing graphene. Optimized structures of PF_6^- intercalation at three different sites with three fluorine atoms facing graphene: (c) S1, (d) S2, (e) S3. RE is the relative energy of the stable sites in eV units. Phosphorus, fluorine and carbon atoms are represented by pink, yellow and grey spheres, respectively.

3.2. System setup

Staging phenomenon is the characteristic feature of layered materials. GICs follow staging mechanism where guest species form repeating patterns between the graphitic layers. This staging mechanism can be well described by two types of forces present during intercalation, one is attractive forces between the graphite layers and second is the repulsive forces between the intercalant species present in the same gallery. The filling of host gallery with the incoming intercalant species is determined by these two forces. If the energy required to overcome the attractive forces between the graphite layers is higher than the repulsive forces between intercalant species, then the intercalation will be assisted in the same host gallery until all sites are filled and after that the next adjacent host layer starts to fill. In this way, the various resultant stages are labelled with respect to number of layers or number of empty host galleries

between the intercalating molecules. Stage-n system corresponds to the ‘n’ number of graphene layers or ‘n-1’ empty host galleries between two intercalating species.

In a similar way, different stages are also expected to appear in DIBs during the intercalation and de-intercalation of anions into graphite. Therefore, to investigate the staging mechanism of PF_6^- intercalation into graphite, we check the favourability of the formation of different stages for exact same PF_6^- concentration. For this, we have considered the optimized geometries of stage-1, stage-2 and stage-4 systems containing four PF_6^- (Figure 2) and have compared their relative energies. We observe that the stage-4 system is more stable than stage-2 followed by stage-1 for a constant PF_6^- concentration. From these results, we can conclude that the intercalation of PF_6^- into graphite also follows staging mechanism and for a given concentration of PF_6^- , intercalation is favoured into a stage-n having highest possible n value as the energy required to overcome the repulsive forces between the intercalant species is less than the energy required to overcome the van der Waals forces between the graphite layers. And in a similar way like intercalation of PF_6^- into graphite during charging, the staging mechanism is also followed for the de-intercalation during discharge process. Overall, with the help of stability calculations, we could explain the formation of different PF_6^- intercalated stages following the staging mechanism of intercalation/deintercalation that have been observed in several experimental reports on PF_6^- dual-ion batteries during the charge/discharge processes.

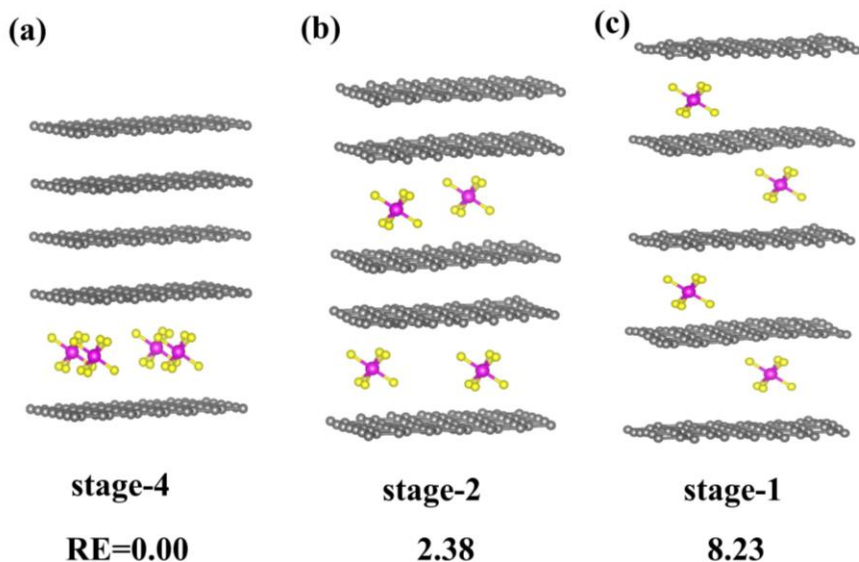


Figure 2. Systematic representation of staging mechanism of PF₆⁻ intercalation into graphite (a) stage-4, (b) stage-2, (c) stage-1. Relative energy (RE) is in eV units for systems containing same PF₆⁻ concentration.

Further, to investigate the staging mechanism in LiPF₆-graphite DIB, we have modelled four stages, stage-1, stage-2, stage-3 and stage-4 of PF₆⁻ intercalated graphite structure. For the calculations of stage-1, stage-2 and stage-4 systems, we have considered a 6×6×2 supercell containing 288 carbon atoms and for stage-3, a 6×6×3 supercell containing 432 carbon atoms is used. Four different concentrations of PF₆⁻ are studied for each stage. Considering the [C₂₈₈(PF₆)_n] formula unit, n values are 4, 8, 12 and 16 for stage-1; 2, 4, 6 and 8 for stage-2; and 1, 2, 3 and 4 for stage-4. Along with that, the formula unit [C₄₃₂(PF₆)_n] is studied for stage-3 with n = 2, 4, 6 and 8. Optimized geometries of all the considered PF₆⁻ intercalated stages are shown in Figure 3.

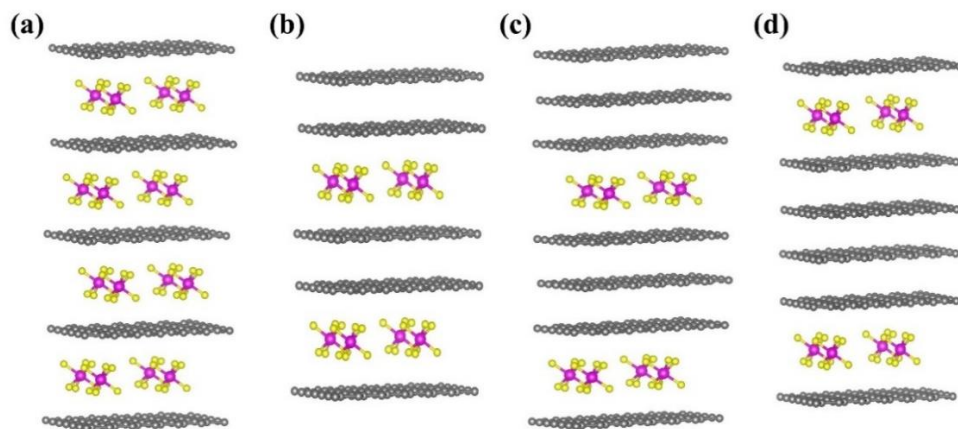


Figure 3. Schematic representation of the optimized geometries of all four different PF_6^- intercalated graphite stages: (a) stage-1, (b) stage-2, (c) stage-3, (d) stage-4.

3.3. Binding energy of PF_6^- intercalated graphite stages

It is very important to determine, whether an intercalation is feasible or not. This feasibility of intercalation can be determined from the stability of intercalated system with the help of binding energy calculations using the following equation,

$$E_{binding} = \frac{E([\text{PF}_6]_x\text{C}_n) - E(\text{C}_n) - xE(\text{PF}_6)}{x}$$

Here, $E([\text{PF}_6]_x\text{C}_n)$ and $E(\text{C}_n)$ represents the total energy values of the graphite system with PF_6^- and without PF_6^- . $E(\text{PF}_6)$ represents the total energy of one PF_6^- molecule obtained by optimizing PF_6^- molecule in a box. Table 1 lists the calculated binding energy values of all four different stages. A higher negative binding energy value shows a more stable intercalation of PF_6^- into graphite. We observe that the binding energy values of all graphite intercalated compounds are negative indicating towards the stability of these PF_6^- intercalated systems. However, in all stages, the first intercalation step is less favourable, and the favourability of intercalation becomes more as PF_6^- concentration further increases. This could be explained as the activation of graphite for the very first

intercalation step, where the partially closed host graphite gallery needs to be activated to accommodate the large sized PF_6^- anion. Whereas, the intercalation becomes easier for the further concentration of PF_6^- as the anions insert into the already expanded graphite galleries. This kind of activation of graphite for the first intercalation steps has also been observed in the several experimental studies of PF_6^- intercalation into graphite [29]. Along with that many other theoretical and experimental reports on various anion intercalation studies (such as AlCl_4^- , TFSI, FSI) have also observed a significant difference between first and other subsequent intercalation steps [30,31]. However, when we particularly compare with AlCl_4^- intercalation, we observe that the AlCl_4^- intercalation requires greater activation of graphitic layers as compared to PF_6^- . It is reflected in the binding energy values of the very first intercalation, which are positive for AlCl_4^- and thus making it difficult to intercalate the large sized AlCl_4^- anions (5.28 Å ionic radius) [32] into partially closed graphite layers [30]. Whereas, in case of PF_6^- intercalation, the activation of graphitic layers is much smoother to accommodate small sized PF_6^- anions (4.36 Å ionic radius) [32], which is clearly reflected from the negative values of binding energy for first intercalation steps resulting into a more favourable intercalation of PF_6^- anions into graphite.

We observe that the intercalation of PF_6^- is accompanied by the volume expansion of graphite by 113 % in stage-1 PF_6^- intercalated system and this calculated value is in accordance to the experimentally obtained volume expansion of 130 %. We have also calculated the gallery height expansion on PF_6^- intercalation for the comparative study with AlCl_4^- and FSI intercalation. The gallery expansion is 114 % in graphite on PF_6^- intercalation, while the observed expansion for AlCl_4^- intercalation (~150-160 %) [14] and FSI intercalation (~134 %) [31] into graphite is quite large. Thus, we can conclude that the LiPF_6 DIBs can provide better cycle stability and could be the promising choice as next generation dual-ion batteries.

Table 1. Binding energy (eV) per PF₆⁻ and average interlayer distance (Å) for all stages with different PF₆⁻ concentration.

Stages	No. of PF ₆ ⁻	Binding energy (eV)	Average interlayer distance (Å)
Stage-1	4	-0.85	6.94
	8	-2.22	7.06
	12	-2.58	7.30
	16	-2.70	7.35
Stage-2	2	-0.88	7.06
	4	-2.32	7.23
	6	-2.71	7.32
	8	-2.86	7.35
Stage-3	2	-0.87	7.07
	4	-2.33	7.26
	6	-2.74	7.34
	8	-2.88	7.37
Stage-4	1	-0.89	7.22
	2	-2.36	7.35
	3	-2.76	7.38
	4	-2.91	7.40

3.4. X-ray diffraction study of PF₆⁻ intercalation into graphite

We have simulated the XRD pattern of optimized supercells of pristine graphite and all four stages (n=1 to 4) as shown in Figure 4. The XRD pattern helps in the determination of structural changes on alteration in the PF₆⁻ concentration. The XRD pattern shows that the PF₆⁻ intercalation into the graphite layers leads some structural changes, and (002) peak of pristine graphite splits into two new peaks corresponding to (00n+1) and (00n+2) planes of stage-n system, indicating the staging behaviour. The stage number of a system is given by the ratio of $d_{(00n+1)}/d_{(00n+2)}$, where $d_{(00n+1)}$ and $d_{(00n+2)}$ are the d-spacing of (00n+1) and (00n+2) planes, respectively, and the interlayer distance (d_i) and periodic repeat distance (I_c) are calculated using the d-spacing values as $d_i=(n+1) \times d_{(00n+1)} - 3.43 \times (n-1)$ and $I_c=(n+1)d_{(00n+1)}=(n+2)d_{(00n+2)}$, respectively. At the fully charged state, XRD pattern indicates the formation of stage-1 system (C₁₈[PF₆]) as confirmed from the d-spacing values of two most intense peaks position $d_{(002)}/d_{(003)} = 3.65/2.43 = 1.50$ with specific capacity of 124 mAhg⁻¹ and the periodic repeat distance and interlayer distance of 7.30 Å ($I_c=2 \times 3.65=3 \times 2.43$). When comparing with FSI intercalated graphite system, we observe that both PF₆⁻ and FSI show the similar staging mechanism, but the interlayer spacing is higher in case of FSI intercalation (7.84 Å) due to its large van der Waals volume (95.00 Å³) than PF₆⁻ (69.00 Å³) [33]. Therefore, exfoliation phenomenon will be less in the case of PF₆⁻ giving long cycle life, which is in accordance with the experimental reports (2000 cycles with 97.9 % capacity retention) [29].

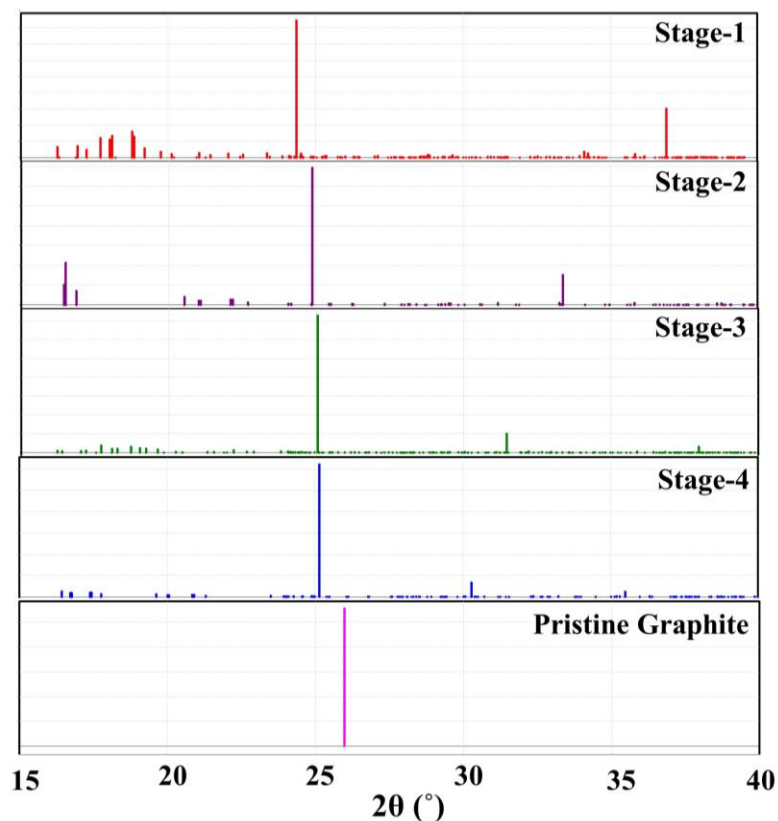


Figure 4. Simulated XRD pattern of pristine graphite and different stages of PF_6^- intercalated graphite supercells. The highest intensity pink coloured peak represents the (002) plane of pristine graphite supercell and the other highest intensity peaks corresponds to the (00n+1) plane and the next high intensity peaks represent the (00n+2) plane of stage-n supercell.

3.5. Electrochemical characteristics

In this section, we have examined the much important electrochemical characteristics such as voltage and storage capacity of LiPF_6 DIB and have made a valuable comparison with the experimental observations. The open circuit voltage is one of the most important electrochemical properties which determines the working suitability of the battery. This LiPF_6 DIB operates with the electrochemical deposition of Li^+ at anode (Lithium) and intercalation/deintercalation of PF_6^- into cathode (graphite), therefore the full cell reaction can be described as:



As shown in the above equation, the reaction mechanism of DIB also involves the contribution from the electrolyte medium. Therefore, battery voltage also depends upon desolvation energy (energy required to form separate anion from electrolyte) and intercalation energy (energy required to intercalate anion into graphite lattice) besides the oxidative potential of graphite.

Cell voltage (V) can be determined by Nernst equation,

$$V = \frac{-\Delta G_{cell}}{zF}$$

Here, z and F are the number of valence electrons and Faraday constant, respectively, and ΔG_{cell} is the change in Gibbs free energy for chemical reaction.

$$\Delta G_{cell} = \Delta H_{cell} - T\Delta S_{cell}$$

$$\Delta G_{cell} = \Delta E_{cell} + P\Delta V_{cell} - T\Delta S_{cell}$$

Here, ΔV_{cell} and ΔS_{cell} are change in volume and entropy for chemical reaction. At 0K, ΔV_{cell} and ΔS_{cell} can be neglected,

$$\Delta G_{cell} = \Delta E_{cell}$$

$$V = \frac{-\Delta E_{cell}}{zF}$$

Therefore, voltage equation can be written as,

$$V = \frac{E(C_n[PF_6]_x) + xE[Li] + 4xE(EMC) - E(C_n) - xE(LiPF_6[EMC]_4)}{x}$$

Where, $E(C_n[PF_6]_x)$, $E(C_n)$ and $E(LiPF_6[EMC]_4)$ corresponds to the total energies of PF_6^- intercalated graphite system, bulk graphite and $LiPF_6[EMC]_4$, respectively. $E[Li]$ gives the total energy value of one lithium atom in a bulk bcc structure. $E(EMC)$ is the total energy of one

EMC molecule obtained by optimizing one EMC molecule in box. $E(\text{LiPF}_6[\text{EMC}]_4)$ is obtained by optimizing $\text{LiPF}_6[\text{EMC}]_4$ as a molecular species due to unavailability of its crystal structure.

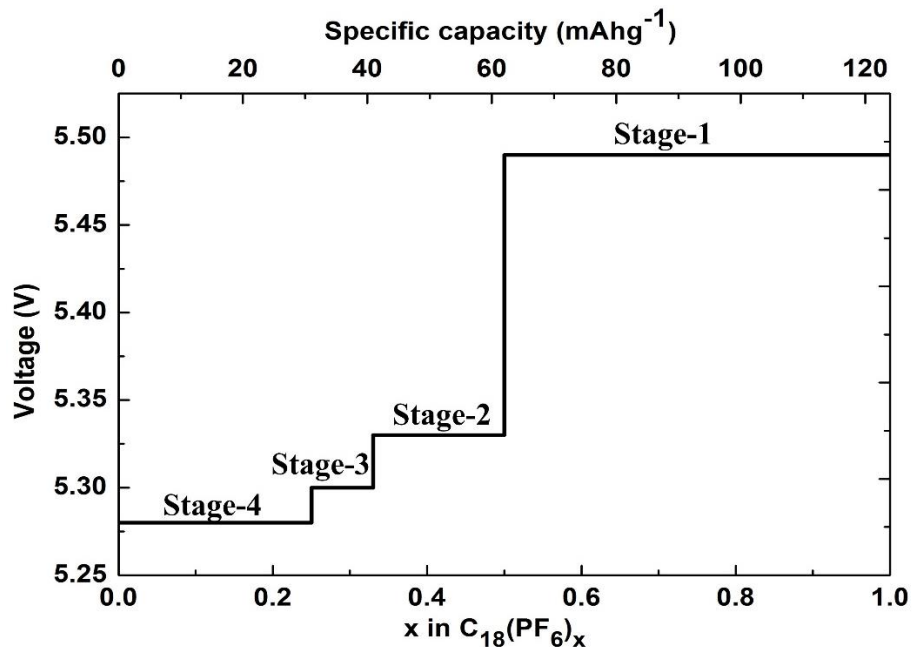


Figure 5. Staging voltage profile diagram for PF_6^- intercalated graphite system.

Figure 5 shows the voltage profile for the PF_6^- intercalation into graphite, *i.e.* moving from low intercalated stages to high intercalated stages and increasing the specific capacity accordingly. It was observed that on going from stage-4 to stage-1, the specific capacity increases from 31.0 mAhg^{-1} ($\text{PF}_6\text{-C}_{72}$) to 124.0 mAhg^{-1} ($\text{PF}_6\text{-C}_{18}$) yielding the voltage steps from 5.28 V to 5.49 V. Voltage obtained for LiPF_6 -graphite DIB is higher than that obtained for FSI-DIB (4.7 V), however both shows the similar staging mechanism and increment in voltage from stage-4 to stage-1 [31]. Our calculated voltage range 5.28-5.49 V is in good accordance with the experimental voltage range of 4.1-5.3 V with the corresponding specific capacity of $\sim 99 \text{ mAhg}^{-1}$ [29].

Specific energy of all the four stages is calculated for the determination of maximum storage capacity. For stage-1, stage-2, stage-3 and stage-4 graphite systems the densities $C_{288}(PF_6)_{16}$, $C_{288}(PF_6)_8$, $C_{432}(PF_6)_8$ and $C_{288}(PF_6)_4$ are considered for specific energy calculations, respectively. Specific energy is calculated by using the equation,

$$E_s = -(E_{C_{18}(PF_6)_x} - E_{C_{18}})/m$$

Here, $E_{C_{18}(PF_6)_x}$ and $E_{C_{18}}$ are the energies of graphite system with and without PF_6^- , and m is the number of carbon atoms in the supercell. Positive value of specific energy indicates the favourable intercalation. Specific energies for stage-1, stage-2, stage-3 and stage-4 are 1.88, 0.94, 0.63 and 0.47 respectively.

Specific capacity can be calculated using the equation given below,

$$C = \frac{nxF}{M_f}$$

where, x and n represent the number of PF_6^- intercalated and number of electrons transferred per PF_6^- molecule, respectively. F gives the faraday constant value and M_f is formula unit mass of intercalating system. Our calculated capacity for stage-1 is 124.0 mAhg^{-1} , which is comparable with experimentally reported value of 99.0 mAhg^{-1} .

3.6. Electronic properties

In this section, we have studied the electronic behaviour of PF_6^- intercalated graphite system and have tried to understand the nature of interaction between the intercalated PF_6^- and graphite host. The constant electronic conductivity of an electrode system is very important getting the optimum battery performance. As we assume that during the intercalation of PF_6^- into graphite, the anion before starting the intercalation releases an electron which is transmitted to current collectors through GICs. Therefore, PF_6-C_n compound should possess electronic conductivity like

other electrode materials. The electronic conductivity can be determined by density of state (DOS) calculations. Figure 6 (a) represents the total density of state (TDOS) and projected density of state (PDOS) of PF_6^- intercalated graphite. It is well known that graphite shows a good in plane electronic conductivity due to the presence of p_z electronic states over the Fermi level and no inter-plane conductivity due to presence of s , p_x , p_y electronic states away from the Fermi level. Upon PF_6^- intercalation into graphite, the electronic conductivity is retained, which can be seen from the electronic states over the Fermi level in Figure 6 (a). This metallic nature of PF_6^- intercalated graphite arises due to some overlap between the $2p$ orbital of F and $2p$ orbital of C.

Finally, we investigate the charge density difference (CDD) calculations to look into the interaction behaviour between the PF_6^- and graphite layers to clarifying the mechanism of PF_6^- intercalation into graphite. This CDD is obtained by using the equation,

$$\rho_{CDD} = \rho^{total} - \sum_i \rho_i^{fragments}$$

Here, ρ^{total} is the total charge density of the system, and $\rho_i^{fragments}$ represents the charge density of individual fragment. Charge density of fragments is calculated using the pseudostructure in which the fragments remains in the same structure as that in total structure, but other parts are deleted. Figure 6 (b) represents the charge density difference plot, where the yellow colour represents the electronic density accumulation and the cyan colour represents the electronic density depletion. From Figure 6 (b) it is found that, the valence electron density of the graphene layers is transferred to the PF_6^- molecule. Therefore, there is net gain of electronic charge around F atoms of PF_6^- and net loss of electronic charge around neighbouring C atoms of graphite indicating towards the ionic character of bonding between the F atoms of PF_6^- molecule and the facing carbon atoms of the graphene layer.

For the quantitative determination of charge transfer, Bader charge analysis is performed. Upon intercalation of PF_6^- into graphite, graphene layers act as the electron donor by decreasing their atomic charge per atom and PF_6^- molecule plays the role of electron acceptor by increasing the atomic charge per atom of F from $-0.63 |e|$ (in isolated state) to $-0.80 |e|$ in GIC. On intercalation, one PF_6^- molecule accepts $\sim -0.97 |e|$ charge from graphite, which clearly concludes the electrochemical oxidation of graphite upon PF_6^- intercalation.

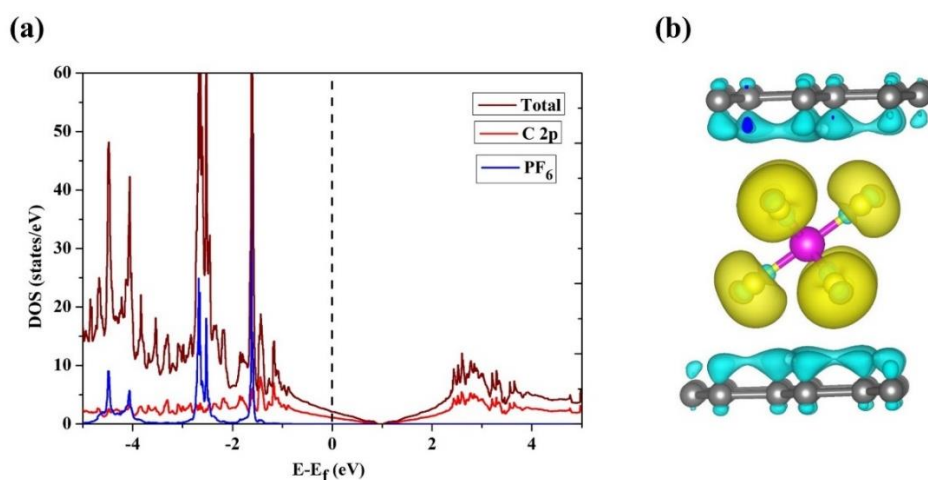


Figure 6. (a) Total and projected DOS of PF_6^- intercalated graphite with Fermi level at zero indicated by dotted line. (b) Isosurface ($0.002 |e| \text{ \AA}^{-3}$) for the charge density difference for PF_6^- intercalated graphite system. Here, the yellow colour represents the electronic density accumulation and the cyan colour represents the electronic density depletion.

3.7. PF_6^- diffusion and energy profile along minimum energy paths

The charging/discharging rate of a DIB depends critically on the speed at which involved ions migrate through electrolyte and electrodes. Therefore, an encouraging strategy to create excellent performance battery is to develop new electrode materials with high electrical conductivity for fast electron transfer and low diffusion barrier for fast ion transfer, which depends upon the mobility of intercalated ions. Here, this mobility is

quantitatively estimated from the diffusion of PF_6^- in the graphite lattice. The diffusion of intercalant PF_6^- in graphite is limited to the 2-dimensional plane due to layered structure of graphite. To find the motion of PF_6^- in graphite lattice, we have considered three different MEPs connecting the two most stable top sites and calculated the corresponding diffusion barrier using CI-NEB method [28]. These MEPs along with their energy profile are shown in Figure 7. Before starting the CI-NEB calculations, structures of initial and final image are fully relaxed, and seven images are inserted between initial and final image. In the path-1 direction, PF_6^- diffusion in graphite lattice is required to overcome a small energy barrier of 0.15 eV. Similarly, the energy barriers for PF_6^- diffusion along path-2 and path-3 are 0.16 and 0.14 eV, respectively. So, the optimal path for PF_6^- diffusion in graphite is path-3. Our results show that the energy barrier of PF_6^- diffusion is quite small compared to the alkali cations (like Li, Na) (0.2-0.4 eV) [34,35] and AlCl_4 (0.33 eV) diffusions in graphite. Therefore, we can say that the diffusion barrier is low enough to provide a trouble-free diffusion for large sized PF_6^- anions in graphite cathode.

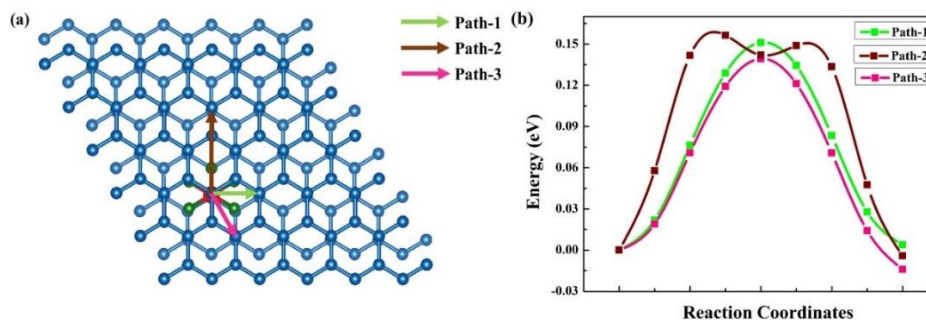


Figure 7. (a) Systematic representation of optimized diffusion pathways of PF_6^- in graphite and (b) involved energy barriers corresponding to the diffusion pathways.

Chapter 4

Conclusion

Based on the first principle calculations, we have systematically studied the staging mechanism of PF_6^- intercalation in graphite to investigate charge transfer mechanism, diffusion barrier and electrochemical properties like voltage and specific capacity. We have modelled four different stages (stage-1, stage-2, stage-3 and stage-4) of PF_6^- intercalated graphite to explore the staging mechanism and to examine the electrochemical properties. On studying the binding characteristics of PF_6^- in graphite, we observe that PF_6^- prefers to be in its energetically octahedral form on intercalation due to van der Waals compressive interaction between the graphite layers. Simultaneously, the interlayer spacing between the graphite layers increases from 3.34 to 7.35 Å on intercalation of PF_6^- , which could result into trouble free diffusion of PF_6^- in graphite. Our diffusion calculations using CI-NEB methods supports this fact and we observe quite small diffusion barrier of 0.14 eV for PF_6^- diffusion inside graphite. Our relative energy calculation of different stages of PF_6^- intercalated system show that during charging first the stage-4 system is formed then stage-3, stage-2 and stage-1, which is also well supported by our simulated XRD patterns. Our simulated XRD patterns confirm that PF_6^- intercalation takes place via the staging mechanism. The smaller XRD simulated interlayer distance observed for PF_6^- intercalation compared to FSI indicates towards decreased exfoliation of graphite cathode for PF_6^- intercalation and an overall increased cycle stability of LiPF_6 -graphite DIB battery. Moreover, our calculated voltage range (5.28-5.49 V) and specific capacity value (124.0 mAhg^{-1}) are in well accordance with the experimentally reported values. The semi-metallic nature of graphite and metallic nature of PF_6^- intercalated graphite provide the evidences for good electronic conductivity, which is crucial for electrode material. The charge density

difference calculations and quantitative Bader charge analysis show that $\sim -0.97 |e|$ charge is transferred from carbon atoms of intercalating material (graphite) to PF_6^- indicating towards the electrochemical oxidation of graphite on PF_6^- intercalation and confirming that PF_6^- intercalation is a charging process. All these results provide in-depth understanding of interaction behaviour of PF_6^- and graphite and help in explaining the role of staging mechanism to obtain precise electrochemical properties such as voltage and storage capacity for LiPF_6 -graphite DIBs.

5. References

- [1] Wang M., Tang Y. (2018), A Review on the Features and Progress of Dual-Ion Batteries, *Adv. Energy Mater.*, 8, 1703320 (<https://doi.org/10.1002/aenm.201703320>)
- [2] Rüdorff W., Hofmann U. (1938), Über Graphitsalze, *Zeitschrift für anorganische und allgemeine Chemie*, 238, 1–50
- [3] Zhang X., Tang Y., Zhang F., Lee C.-S. (2016), A Novel Aluminum-Graphite Dual-Ion Battery, *Adv. Energy Mater.*, 6, 1502588 (<https://doi.org/10.1002/aenm.201502588>)
- [4] Tong X., Zhang F., Chen G., Liu X., Gu L., Tang Y. (2018), Core-Shell Aluminum@Carbon Nanospheres for Dual-Ion Batteries with Excellent Cycling Performance under High Rates, *Adv. Energy Mater.*, 8, 1701967 (<https://doi.org/10.1002/aenm.201701967>)
- [5] Sheng M., Zhang F., Ji B., Tong X., Tang Y. (2017), A Novel Tin-Graphite Dual-Ion Battery Based on Sodium-Ion Electrolyte with High Energy Density, *Adv. Energy Mater.*, 7, 1601963 (<https://doi.org/10.1002/aenm.201601963>)
- [6] Seel J. A., Dahn J. R. (2000), Electrochemical Intercalation of PF₆ into Graphite, *J. Electrochem. Soc.*, 147, 892 (<https://doi.org/10.1149/1.1393288>)
- [7] Deunf É., Moreau P., Quarez É., Guyomard D., Dolhem F., Poizot P. (2016), Reversible Anion Intercalation in a Layered Aromatic Amine: A High-Voltage Host Structure for Organic Batteries, *J. Mater. Chem. A*, 4, 6131–6139 (<https://doi.org/10.1039/C6TA02356H>)
- [8] Carlin R. T. (1994), Dual Intercalating Molten Electrolyte Batteries, *J. Electrochem. Soc.*, 141, L73 (<https://doi.org/10.1149/1.2055041>)
- [9] Sutto T. E., Duncan T. T., Wong T. C. (2009), X-Ray Diffraction Studies of Electrochemical Graphite Intercalation Compounds of

- Ionic Liquids, *Electrochimica Acta*, 54, 5648–5655 (<https://doi.org/10.1016/j.electacta.2009.05.026>)
- [10] Liao H.-J., Chen Y.-M., Kao Y.-T., An J.-Y., Lai Y.-H., Wang D.-Y. (2017), Freestanding Cathode Electrode Design for High-Performance Sodium Dual-Ion Battery, *J. Phys. Chem. C*, 121, 24463–24469 (<https://doi.org/10.1021/acs.jpcc.7b08429>)
- [11] Ji B., Zhang F., Wu N., Tang Y. (2017), A Dual-Carbon Battery Based on Potassium-Ion Electrolyte, *Adv. Energy Mater.*, 7, 1700920 (<https://doi.org/10.1002/aenm.201700920>)
- [12] Fan L., Liu Q., Chen S., Xu Z., Lu B. (2017), Soft Carbon as Anode for High-Performance Sodium-Based Dual Ion Full Battery, *Adv. Energy Mater.*, 7, 1602778 (<https://doi.org/10.1002/aenm.201602778>)
- [13] Li Q., Bjerrum N. J. (2002), Aluminum as Anode for Energy Storage and Conversion: A Review, *Journal of Power Sources*, 110, 1–10 ([https://doi.org/10.1016/S0378-7753\(01\)01014-X](https://doi.org/10.1016/S0378-7753(01)01014-X))
- [14] Read J. A., Cresce A. V., Ervin M. H., Xu K. (2014), Dual-Graphite Chemistry Enabled by a High Voltage Electrolyte, *Energy Environ. Sci.*, 7, 617–620 (<https://doi.org/10.1039/C3EE43333A>)
- [15] Wang M., Zhang F., Lee C.-S., Tang Y. (2017), Low-Cost Metallic Anode Materials for High Performance Rechargeable Batteries, *Adv. Energy Mater.*, 7, 1700536 (<https://doi.org/10.1002/aenm.201700536>)
- [16] Xi X.-T., Li W.-H., Hou B.-H., Yang Y., Gu Z.-Y., Wu X.-L. (2019), Dendrite-Free Lithium Anode Enables the Lithium//Graphite Dual-Ion Battery with Much Improved Cyclic Stability, *ACS Appl. Energy Mater.*, 2, 201–206 (<https://doi.org/10.1021/acsaem.8b01764>)
- [17] Xu K. (2004), Nonaqueous Liquid Electrolytes for Lithium-Based Rechargeable Batteries, *Chem. Rev.*, 104, 4303–4418 (<https://doi.org/10.1021/cr030203g>)

- [18] Xu K., von Cresce A. (2011), Interfacing Electrolytes with Electrodes in Li Ion Batteries, *J. Mater. Chem.*, 21, 9849 (<https://doi.org/10.1039/c0jm04309e>)
- [19] Miyoshi S., Akbay T., Kurihara T., Fukuda T., Staykov A. T., Ida S., Ishihara T. (2016), Fast Diffusivity of PF_6^- Anions in Graphitic Carbon for a Dual-Carbon Rechargeable Battery with Superior Rate Property, *J. Phys. Chem. C*, 120, 22887–22894 (<https://doi.org/10.1021/acs.jpcc.6b07957>)
- [20] Kresse G., Furthmüller J. (1996), Efficient Iterative Schemes for Ab Initio Total-Energy Calculations Using a Plane-Wave Basis Set, *Phys. Rev. B*, 54, 11169–11186 (<https://doi.org/10.1103/PhysRevB.54.11169>)
- [21] Chen Y., Peng F., Yan Y., Wang Z., Sun C., Ma Y. (2013), Exploring High-Pressure Lithium Beryllium Hydrides: A New Chemical Perspective, *J. Phys. Chem. C*, 117, 13879–13886 (<https://doi.org/10.1021/jp404046g>)
- [22] Perdew J. P., Burke K., Ernzerhof M. (1996), Generalized Gradient Approximation Made Simple, *Phys. Rev. Lett.*, 77, 3865–3868 (<https://doi.org/10.1103/PhysRevLett.77.3865>)
- [23] Blöchl P. E. (1994), Projector Augmented-Wave Method, *Phys. Rev. B*, 50, 17953–17979 (<https://doi.org/10.1103/PhysRevB.50.17953>)
- [24] Grimme S., Antony J., Ehrlich S., Krieg H. (2010), A Consistent and Accurate Ab Initio Parametrization of Density Functional Dispersion Correction (DFT-D) for the 94 Elements H-Pu, *The Journal of Chemical Physics*, 132, 154104 (<https://doi.org/10.1063/1.3382344>)
- [25] Henkelman G., Arnaldsson A., Jónsson H. (2006), A Fast and Robust Algorithm for Bader Decomposition of Charge Density, *Computational Materials Science*, 36, 354–360 (<https://doi.org/10.1016/j.commatsci.2005.04.010>)

- [26] Bader R. F. W. (1991), A Quantum Theory of Molecular Structure and Its Applications, *Chem. Rev.*, 91, 893–928 (<https://doi.org/10.1021/cr00005a013>)
- [27] Sanville E., Kenny S. D., Smith R., Henkelman G. (2007), Improved Grid-Based Algorithm for Bader Charge Allocation, *J. Comput. Chem.*, 28, 899–908 (<https://doi.org/10.1002/jcc.20575>)
- [28] Mills G., Jónsson H., Schenter G. K. (1995), Reversible Work Transition State Theory: Application to Dissociative Adsorption of Hydrogen, *Surface Science*, 324, 305–337 ([https://doi.org/10.1016/0039-6028\(94\)00731-4](https://doi.org/10.1016/0039-6028(94)00731-4))
- [29] Wang G., Yu M., Wang J., Li D., Tan D., Löffler M., Zhuang X., Müllen K., Feng X. (2018), Self-Activating, Capacitive Anion Intercalation Enables High-Power Graphite Cathodes, *Adv. Mater.*, 30, 1800533 (<https://doi.org/10.1002/adma.201800533>)
- [30] Bhauriyal P., Mahata A., Pathak B. (2017), The Staging Mechanism of AlCl₄ Intercalation in a Graphite Electrode for an Aluminium-Ion Battery, *Phys. Chem. Chem. Phys.*, 19, 7980–7989 (<https://doi.org/10.1039/C7CP00453B>)
- [31] Kravchyk K. V., Bhauriyal P., Piveteau L., Guntlin C. P., Pathak, B., Kovalenko M. V. (2018), High-Energy-Density Dual-Ion Battery for Stationary Storage of Electricity Using Concentrated Potassium Fluorosulfonylimide, *Nat Commun*, 9, 4469 (<https://doi.org/10.1038/s41467-018-06923-6>)
- [32] Zhou X., Liu Q., Jiang C., Ji B., Ji xiulei, Tang Y., Cheng H.-M. (2019), Beyond Conventional Batteries: Strategies towards Low-Cost Dual-Ion Batteries with High Performance, *Angew. Chem. Int. Ed.* (<https://doi.org/10.1002/anie.201814294>)
- [33] Han H.-B., Zhou S.-S., Zhang D.-J., Feng S.-W., Li L.-F., Liu K., Feng W.-F., Nie J., Li H., Huang X.-J. (2011), Lithium Bis(Fluorosulfonyl)Imide (LiFSI) as Conducting Salt for Nonaqueous Liquid Electrolytes for Lithium-Ion Batteries:

Physicochemical and Electrochemical Properties, *Journal of Power Sources*, 196, 3623–3632 (<https://doi.org/10.1016/j.jpowsour.2010.12.040>)

- [34] Nobuhara K., Nakayama H., Nose M., Nakanishi S., Iba H. (2013), First-Principles Study of Alkali Metal-Graphite Intercalation Compounds, *Journal of Power Sources*, 243, 585–587 (<https://doi.org/10.1016/j.jpowsour.2013.06.057>)
- [35] Persson K., Hinuma Y., Meng Y. S., Van der Ven A., Ceder G. (2010), Thermodynamic and Kinetic Properties of the Li-Graphite System from First-Principles Calculations, *Phys. Rev. B*, 82, 125416 (<https://doi.org/10.1103/PhysRevB.82.125416>)

